A novel energy mapping approach for CT-based attenuation correction in PET

B. Teimourian
Faculty of Physics and Nuclear Engineering, Amir Kabir University of Technology (Tehran Polytechnic), P.O. Box 4413-15875, Tehran, Iran and Research Center for Science and Technology in Medicine, Tehran University of Medical Sciences, P.O. Box 14155-6447, Tehran, Iran

M. R. Ay[a)]
Research Center for Science and Technology in Medicine, Tehran University of Medical Sciences, P.O. Box 14155-6447, Tehran, Iran; Research Institute for Nuclear Medicine, Tehran University of Medical Sciences, P.O. Box 14185-615, Tehran, Iran; and Department of Medical Physics and Biomedical Engineering, Tehran University of Medical Sciences, P.O. Box 14185-615, Tehran, Iran

M. Shamsaie Zafarghandi
Faculty of Physics and Nuclear Engineering, Amir Kabir University of Technology (Tehran Polytechnic), P.O. Box 4413-15875, Tehran, Iran

P. Ghafarian
Telemedicine Research Center, NRITLD, Masih Daneshvari Hospital, Shahid Beheshti University of Medical Sciences, Tehran, Iran and Chronic Respiratory Diseases Research Center, NRITLD, Masih Daneshvari Hospital, Shahid Beheshti University of Medical Sciences, P.O. Box 19556, Tehran, Iran

H. Ghadiri
Research Center for Science and Technology in Medicine, Tehran University of Medical Sciences, P.O. Box 14155-6447, Tehran, Iran and Department of Medical Physics and Biomedical Engineering, Tehran University of Medical Sciences, P.O. Box 14185-615, Tehran, Iran

H. Zaidi
Division of Nuclear Medicine and Molecular Imaging, Geneva University Hospital, CH-1211 Geneva, Switzerland; Geneva Neuroscience Center, Geneva University, CH-1211 Geneva, Switzerland; and Department of Nuclear Medicine and Molecular Imaging, University Medical Center Gronigen, University of Groningen, 9700 RB Groningen, The Netherlands

(Received 22 September 2011; revised 31 January 2012; accepted for publication 26 February 2012; published 23 March 2012)

Purpose: Dual-energy CT (DECT) is arguably the most accurate energy mapping technique in CT-based attenuation correction (CTAC) implemented on hybrid PET/CT systems. However, this approach is not attractive for clinical use owing to increased patient dose. The authors propose a novel energy mapping approach referred to as virtual DECT (VDECT) taking advantage of the DECT formulation but using CT data acquired at a single energy (kV_P). For this purpose, the CT image acquired at one energy is used to generate the CT image at a second energy using calculated kV_P conversion curves derived from phantom studies.

Methods: The attenuation map (μ-map) at 511 keV was generated for the XCAT phantom and clinical studies using the bilinear, DECT, and VDECT techniques. The generated μ-maps at 511 keV are compared to the reference derived from the XCAT phantom serving as ground truth. PET data generated from a predefined activity map for the XCAT phantom were then corrected for attenuation using μ-maps generated using the different energy mapping approaches. In addition, the generated μ-maps using the above described methods for a cylindrical polyethylene phantom containing different concentrations of K_2HPO_4 in water were compared to actual attenuation coefficients. Likewise, CT images of five clinical whole-body studies were used to generate μ-maps using the various energy-mapping approaches were compared with μ-maps acquired at 511 keV using $^{68}Ge/^{68}Ga$ rod sources for the clinical studies.

Results: The results of phantom studies demonstrate that the proposed method is more accurate than the bilinear technique. All three μ-maps yielded almost similar results for soft and lung tissues whereas for bone tissues, the DECT and the VDECT methods produced a much smaller mean relative difference (3.0% and 2.8%, respectively) than the bilinear approach (11.8%). Likewise, the comparison of PET images corrected for attenuation using the various methods showed that the proposed method provides better accuracy (6.5%) than the bilinear method (13.4%). Clinical studies further demonstrated that, compared to the bilinear method, the VDECT approach has better agreement for bony structures with the DECT technique (1.5% versus 8.9%) and transmission scanning (8.8% versus 17.7%).

 0094-2405/2012/39(4)/2078/12/$30.00

Conclusions: It was concluded that the proposed method outperforms the bilinear method especially in bony structures. Further evaluation using a large clinical PET/CT database is underway to evaluate the potential of the technique in a clinical setting. © *2012 American Association of Physicists in Medicine*. [http://dx.doi.org/10.1118/1.3694108]

Key words: PET/CT, attenuation correction, attenuation map, energy-mapping, dual-energy CT

I. INTRODUCTION

Positron emission tomography (PET) produces images depicting the time varying biodistribution of positron-emitting probes in the patient's body. The resulting PET images are interpreted visually to assess the physiologic function of tissues, organs, and organ systems or can eventually be evaluated quantitatively to measure biochemical and physiologic processes *in vivo*. However, several physical factors can degrade image quality and quantitative accuracy of PET images including the detection of Compton Scattered photon,[1] patient motion,[2] attenuation of photons,[3] partial volume effect,[4] parallax effect,[5] positron range,[6] and annihilation photon acollinearity.[7] In particular, attenuation of photons in tissues affects both visual quality and quantitative accuracy of PET images. Therefore, accurate attenuation correction is necessary for improving image quality, enhancing lesion detectability, and for enabling quantitative analysis, thus allowing better management of patients in clinical oncology.[8,9]

Attenuation correction requires the availability of an attenuation map (μ-map) which can be derived using either radionuclide or x-ray transmission scanning. Radionuclide transmission scanning is commonly implemented on standalone PET systems where the attenuation map is generated from either positron-emitting (^{68}Ga/^{68}Ge) rod sources or single-photon emitting (^{137}Cs) point sources, which rotate around the patient. The main advantage of this approach is that the energy of photons emitted from both sources is equal or very close to the energy of annihilation photons. The commercial introduction of combined PET/CT units stimulated the development of CT-based attenuation correction (CTAC).[10]

CTAC has several advantages compared to radionuclide transmission scanning, including the generation of a noise free μ-map, reduction of total scanning time, and the ability to collect uncontaminated postinjection transmission scans.[11] Despite these advantages, the technique increases the radiation dose delivered to the patient compared to radionuclide transmission scanning and suffers from many other drawbacks.[12]

There are two important issues that should be considered when generating a μ-map using CTAC: First, attenuation coefficients in CT images are measured at lower energies (effective energy ~55–80 keV) compared to annihilation photons' energy in PET (511 keV). Second, the x-ray source in CT emits photons with a broad energy spectrum varying from 40 keV to 140 keV,[13] whereas the annihilation photons emitted by PET tracers are almost monochromatic (511 keV). Therefore, an accurate energy mapping method that converts attenuation coefficients measured at CT energies to equivalent values at 511 keV is essential.[14] Several energy-mapping techniques were proposed in the literature including: scaling,[15] segmentation,[11] hybrid (segmentation/scaling),[10] bilinear,[14,16] quadratic,[17] and the dual-energy technique.[18,19]

Among the above referenced methods, the dual-energy technique presents a high accuracy, since it uses dual kV_P CT scans to estimate the μ-map at 511 keV.[17,20] However, the technique bears many inherent drawbacks including the additional radiation dose to the patient which makes it impractical for clinical use.[21] In this work, we propose a new method allowing the implementation of the dual-energy approach using only a single energy CT image. The aim of this virtual dual-energy method is to generate a more accurate μ-map especially in bony tissues compared to the common bilinear method implemented on commercial PET/CT scanners without delivering a higher radiation dose to the patient.

II. MATERIALS AND METHODS

II.A. X-ray CT and PET/CT scanners

The 64-slice LightSpeed VCT scanner (GE Healthcare, Waukesha, WI) equipped with highlight (Y2Gd2O3:Eu) ceramic scintillators was used for both phantom and clinical studies. This third generation CT scanner has a 540-mm source-to-isocenter and 950-mm source-to-detector distances, 58 368 individual detector elements arranged in 64 rows of 0.625 mm thickness at isocenter, each containing 888 active patient elements and 24 reference elements. The scanner is equipped with the Performix Pro anode grounded metal-ceramic tube unit, which uses 56° fan angle, 7° target angle and minimum inherent filtration of 3.25 mm Al and 0.1 mm Cu at 140 kV_P.

Five clinical whole-body CT images and their corresponding transmission images, produced using ^{68}Ge/^{68}Ga rod sources, were acquired on the Discovery LS (DLS) PET/CT scanner (GE Healthcare Technologies, Waukesha, WI). This scanner has the capability of producing both radionuclide- and CT-based μ-maps. The detector blocks use BGO crystals of dimensions $4 \times 8 \times 30$ mm^3 in the tangential, axial, and radial directions, respectively, arranged into 18 rings with 672 crystals per ring.

II.B. Energy-mapping methods

Since CT images are scaled in Hounsfield units (HU), accurate conversion from CT numbers to linear attenuation coefficient at 511 keV ($\mu_{511\text{keV}}$) is required by the CTAC procedure. Several energy-mapping approaches were proposed including scaling, segmentation, hybrid (scaling/segmentation), bilinear, quadratic, and dual-energy decomposition.[17] This work compares the dual-energy and proposed virtual

dual-energy approaches to the bilinear technique as the most commonly used technique on commercial PET/CT scanners.

II.B.1. Bilinear approach

The bilinear calibration curve is obtained by relating CT numbers of three reference points including air, water, and cortical bone to the corresponding μ values at 511 keV. Hence, the HUs in CT images are divided into two regions ($-1000 < \mathrm{HU} \leq 0$ and $\mathrm{HU} > 0$) and the experimentally derived conversion equations used to convert CT numbers to $\mu_{511\mathrm{keV}}$ for each regions.[14]

II.B.2. Dual-energy (DECT) approach

Since $\mu_{511\mathrm{keV}}$ reflects the sum of photoelectric absorption and Compton scattering components, the transformation of CT images expressed in HUs to $\mu_{511\mathrm{keV}}$ cannot be performed perfectly using a single $\mathrm{kV_P}$ CT scan.[20] In the dual-energy technique, the individual photoelectric and Compton scattering contributions are determined using CT images acquired at two different energies.[18] The main advantage of this approach is the generation of an accurate μ-map at 511 keV especially in the presence of high-Z materials including bone, contrast agents, and metallic objects.[18,19]

II.B.3. Virtual dual-energy (VDECT) approach

Although the DECT method produces the most accurate attenuation map compared to other energy-mapping techniques, its routine clinical exploitation is hampered by a substantial increase of patient dose, since two CT scans acquired at different $\mathrm{kV_P}$ are required. The VDECT technique uses a single CT scan acquired at one tube voltage and its algorithmic implementation requires the following steps. First, CT images at 140 $\mathrm{kV_P}$ are acquired. Second, using this CT image and $\mathrm{kV_P}$ conversion equations obtained from the phantom experiment described below, the corresponding CT image at 80 $\mathrm{kV_P}$ is generated. It should be emphasized that since the noise in CT images is lower at high $\mathrm{kV_P}$, CT images at 80 $\mathrm{kV_P}$ were derived from 140 $\mathrm{kV_P}$. Third, The DECT technique described by Guy *et al.*[18] is applied using the acquired and generated CT images. In other words, the CT image acquired at 140 $\mathrm{kV_P}$ is converted to an attenuation map at 511 keV by applying $\mathrm{kV_P}$ conversion equations and dual-energy formulation[18] (see Appendix A).

II.C. Phantom studies

An experimental phantom and anthropomorphic computerized anatomical model were used in this work.

II.C.1. RANDO Alderson phantom

The RANDO Alderson phantom (Radiology Support Devices, Inc., Long Beach, CA) consists of bone, lung, and soft tissue compositions formulated to mimic radiation interaction processes with biological tissues in the diagnostic and therapeutic energy range. Tissue-equivalent materials use human tissue composition data given in ICRU 44 report.[22] This arrangement provides anatomical properties similar to the human body, suitable for mimicking whole-body PET/CT studies. The phantom is available in male and female models.

The RANDO Alderson phantom was scanned on a LightSpeed VCT scanner (GE Healthcare, Waukesha, WI) at 80 and 140 $\mathrm{kV_P}$ tube voltages and tube current of 300 mA. Representative CT images of this phantom acquired at 140 $\mathrm{kV_P}$ are shown in Fig. 1. The CT images acquired at two energies were used to derive $\mathrm{kV_P}$ conversion curves for the three tissue types, namely, soft tissue, lung, and bone. For this purpose, over 400 ROIs were defined on both CT images using AMIDE,[23] and the mean CT number of each ROI at 80 $\mathrm{kV_P}$ was plotted against the corresponding value at 140 $\mathrm{kV_P}$ for the three different regions including lung ($\mathrm{HU} \leq -100$), soft tissue ($-100 < \mathrm{HU} < 200$), and bone ($\mathrm{HU} \geq 200$).[21] Fitting curves referred to as $\mathrm{kV_P}$ conversion curves were then calculated for each tissue type and the corresponding linear regression equations obtained from each curve (Fig. 2). Since biological tissues have almost similar interaction properties at CT tube voltages close to each other, this classification improves the precision of the resulting $\mathrm{kV_P}$ conversion curves and corresponding equations. The obtained $\mathrm{kV_P}$ conversion equations allow the conversion of CT images acquired at 140 $\mathrm{kV_P}$ to CT images at 80 $\mathrm{kV_P}$ and vice versa.

II.C.2. Polyethylene phantom

A polyethylene cylindrical phantom (250 ± 0.5 mm diameter) consisting of 16 cylindrical holes (20 ± 0.5 mm diameter) with four holes in the middle (5 ± 0.5 mm diameter) filled with air was constructed. One of the 16 holes was filled with water and the rest with various concentrations of K_2HPO_4 in water ranging between 60 and 1800 mg/cc to simulate different biological tissues.

This phantom was scanned on the LightSpeed VCT scanner at 80 and 140 $\mathrm{kV_P}$s and tube current of 400 mA with 1-s rotation speed. The acquired CT image at 140 $\mathrm{kV_P}$ was converted to CT image at 80 $\mathrm{kV_P}$ to validate the $\mathrm{kV_P}$ conversion equations obtained from the RANDO Alderson phantom. Thereafter, the generated CT image was compared to the acquired CT image at 80 $\mathrm{kV_P}$. In addition, the acquired CT images were used to assess the accuracy of μ-maps generated using the bilinear, DECT, and VDECT energy-mapping methods. The actual μ at 511 keV for each concentration of

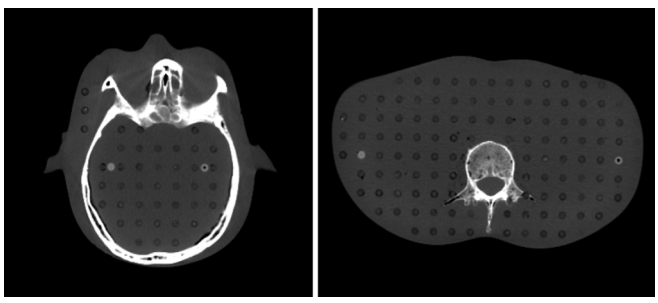

FIG. 1. Transaxial views of representative CT images of the RANDO Alderson phantom at 140 $\mathrm{kV_P}$.

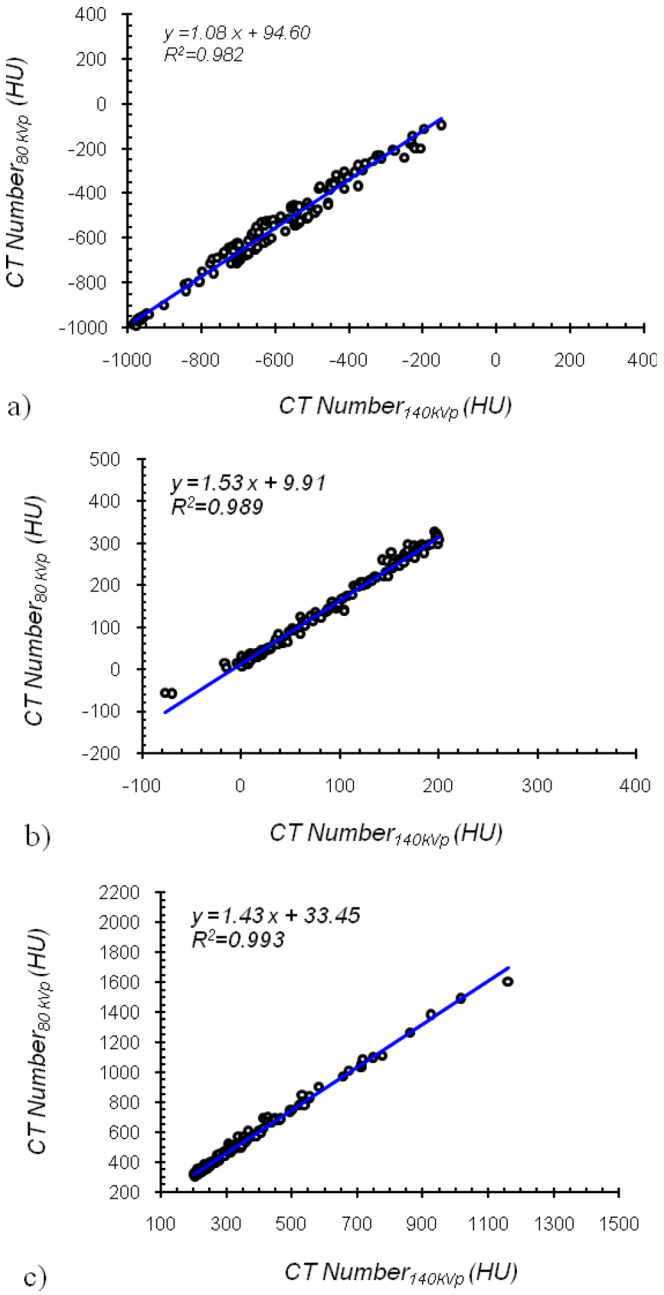

FIG. 2. Conversion curves obtained from CT images of the RANDO Alderson phantom acquired at 80 and 140 kV_P for: (a) lung, (b) soft tissue, and (c) bone.

the K_2HPO_4 solution was computed using the XCOM photon cross-section library,[24] which served as reference.

II.C.3. 4D XCAT model

The 4D extended cardiac-torso XCAT model is a realistic whole-body computerized model representing the human anatomy based on nonuniform rational B-spline surfaces (NURBS).[25] This voxelized model allows simultaneous generation of attenuation and activity maps with any desired biodistribution. Human tissue compositions were taken from ICRU report 44.[22]

Whole-body attenuation maps at 60, 82 (corresponding to the effective energy of CT at 80 and 140 kV_P, respectively),[14] and 511 keV were generated and used to evaluate the accuracy of the proposed method in terms of attenuation map estimation. In addition, μ-maps at 511 keV were generated using the bilinear, DECT, and VDECT approaches and compared to the one derived from the XCAT phantom serving as reference. Likewise, activity maps in the thorax containing five lesions located at different organs (liver, lung, kidney, spine bone, and scapula bone) and corresponding attenuation maps at 60, 82 and 511 keV were used to assess the accuracy of the proposed technique on reconstructed PET images. The matrix size of all images (whether activity or attenuation maps) is 128×128 with a pixel size of 3.125 mm. Simulated PET data were then generated analytically taking into account the effect of photon attenuation and statistical noise. The generated PET sinograms were then corrected for attenuation using the CTAC procedure using bilinear, DECT, and VDECT approaches for energy mapping. Attenuation correction and reconstruction of PET images were performed using the STIR (Software for Tomographic Image Reconstruction) package.[26]

II.D. Clinical studies

Sixteen patients underwent CT scans on the LightSpeed VCT scanner at tube voltages of 80 and 140 kV_Ps. Only one slice was acquired to keep patient dose to a reasonable level. This study was approved by the ethical committee of Tehran University of Medical Sciences (Ethic license number 1432), and all patients gave their written informed consent for participation. CT images of two patients were excluded from the study because of patient motion. First, the data were used to validate kV_P conversion equations obtained from the RANDO Alderson phantom study. For this purpose, CT images at 140 kV_P were converted to CT images at 80 kV_P using these equations. Then, the generated CT images at 80 kV_P (virtual CT images) were compared to actual CT images acquired at the same energy.

Second, clinical CT images were used to evaluate the accuracy of attenuation maps at 511 keV generated using the proposed VDECT method, bilinear, and DECT approaches. Since the DECT technique is arguably the most accurate one, the μ-maps produced using this technique were used as reference. The acquired CT images at 140 kV_P were converted to μ-map using the bilinear method. In addition, CT images at 80 and 140 kV_P were used to apply the DECT technique. Finally, acquired CT images at 140 kV_P and the virtually generated CT image at 80 kV_P were used to create the corresponding VDECT μ-map.

Five whole-body CT images were also selected from the clinical PET/CT database to evaluate the proposed method. For this purpose, attenuation maps produced using both the proposed method and the bilinear technique were compared to transmission images acquired at 511 keV using $^{68}Ge/^{68}Ga$ rod sources on a GE Discovery LS PET/CT scanner.

II.E. Attenuation correction and image reconstruction

Three steps were followed for both clinical and experimental phantom studies to create μ-maps corresponding to

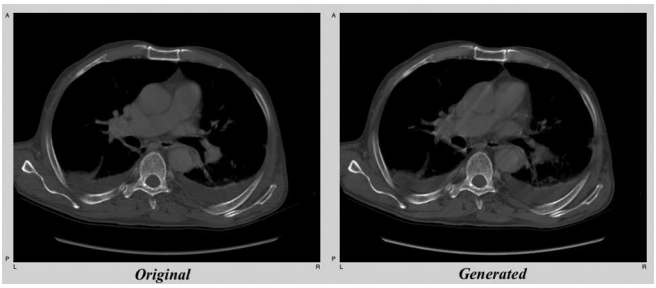

FIG. 3. Original and generated (from 140 kV_P) clinical thoracic CT images at 80 kV_P.

each energy-mapping method. First, CT images (512×512 matrix size) were down-sampled to match PET voxel's size (128×128). Second, the down-sampled CT images were converted to μ-maps at 511 keV using the previously described energy-mapping techniques. Finally, the obtained μ-maps were smoothed using a 5-mm Gaussian kernel to match the resolution of PET images. It should be noted that the smoothing of the five CT data acquired on the DLS scanner was performed using an 8-mm Gaussian kernel to match noisy transmission images.

Since the activity and attenuation maps of the XCAT phantom have the same matrix size (128×128) and the same voxel size (3.125 mm), only energy-mapping step was performed to generate the μ-map at 511 keV. The generated emission sinograms corrected for attenuation using different energy-mapping methods were reconstructed using the ordered subsets expectation maximization OSEM algorithm with six iteration and eight subsets.

II.F. Assessment strategy

For validation of kV_P conversion equations, a region of interest (ROI)-based analysis was used for both clinical and phantom studies. For this purpose, several ROIs were defined in various tissues on the actual CT image at 80 kV_P and the virtually generated CT image at the same energy using kV_P conversion equations. Quantification of the agreement between two algorithms was performed by using Bland and Altman statistical analysis consisting in plotting the difference against the average of the compared methods.[27] The mean CT numbers of each ROI in both CT images were compared using Bland and Altman plots. Eleven ROIs were defined on various organs/tissues of the XCAT phantom, whereas 17 ROIs were delineated on the cylinders containing different concentrations of K_2HPO_4 solutions, water, and air in the polyethylene phantom. The results were then compared to the actual μ calculated using the XCOM photon cross-section library.[24] In addition, 175 ROIs were defined on the 14 clinical CT images consisting of 119 ROIs in soft tissues, 36 ROIs in bones, and 20 ROIs in the lungs.

Another set of ROIs was also defined for quantitative analysis of the proposed method using clinical data. A total number of 117 ROIs were defined on each created μ-map at 511 keV for the 14 slices of clinical CT images consisting of 56 ROIs on soft tissues, 43 ROIs on bones, and 18 ROIs on the lungs. Similarly, 265 ROIs were defined on the different μ-maps of the 5 PET/CT data including 93 ROIs on soft tissues, 51 ROIs on bones, and 121 ROIs on the lungs.

The mean μ_{511keV} for each ROI estimated using the bilinear and VDECT μ-maps was compared to corresponding values of the reference μ-map, i.e., the DECT μ-map for the 14 clinical

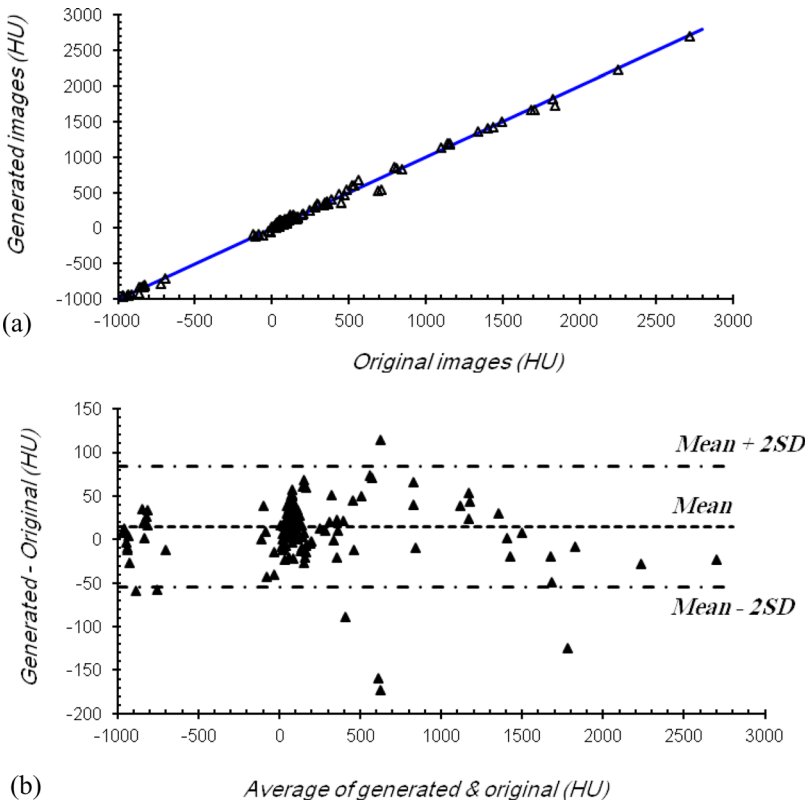

FIG. 4. Correlation plots (a) and Bland and Altman plots (b) showing difference against average HU for each ROI obtained from the original and generated CT images. The middle line is the mean and the upper and lower broken lines are the mean $\pm 2 \times$ SD (standard deviation). The limits of agreement define the 95% confidence interval.

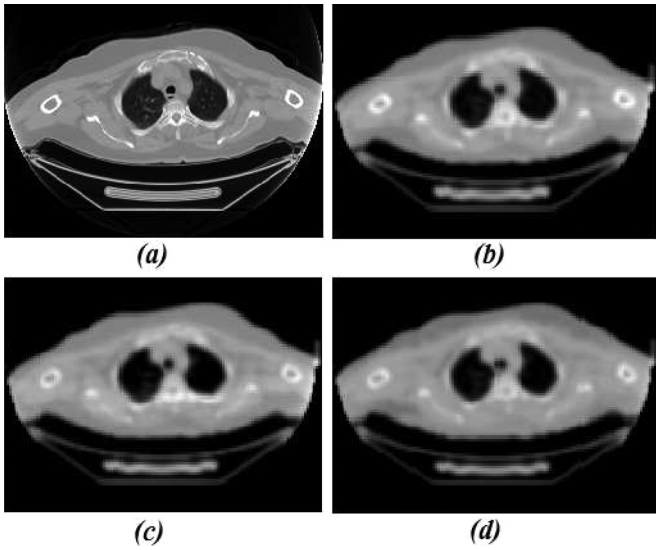

FIG. 5. (a) Original clinical CT image and attenuation maps generated using (b) bilinear, (c) dual-energy (80 and 140 kV_P), and (d) virtual dual-energy mapping approaches.

CT images and the transmission image for the 5 clinical PET/CT images. The percentage relative difference (PRD) was also calculated. In addition, correlation plots between the reference and other energy-mapping approaches were obtained. The Mann–Whitney test was used for statistical analysis.

Similarly, different ROIs were defined on PET images corrected for attenuation using the bilinear, DECT, and VDECT energy-mapping approaches and compared to images corrected using the reference μ-map derived from the XCAT phantom. The mean activity for each ROI was determined and the percentage relative difference between PET images corrected using the bilinear, DECT, and VDECT techniques and the reference were obtained.

III. RESULTS

III.A Clinical studies

Figure 3 shows the original and virtually generated CT images at 80 kV_P of a clinical study. Small mismatches can be observed in the lung region of the virtually generated CT image owing to respiratory mismatch between the original CT image acquired at 80 kV_P and the one acquired at 140 kV_P keeping in mind that the VDECT image is derived from the CT image acquired at 140 kV_P. ROI-based linear regression and Bland–Altman analysis performed on these two sets of CT images are shown in Fig. 4. It can be seen that the CT images generated at 80 kV_P using conversion equations is concordant with the actual CT images acquired at 80 kV_P. Therefore, the kV_P conversion equations present acceptable accuracy for converting clinical CT images acquired at 140 kV_P to corresponding images at 80 kV_P.

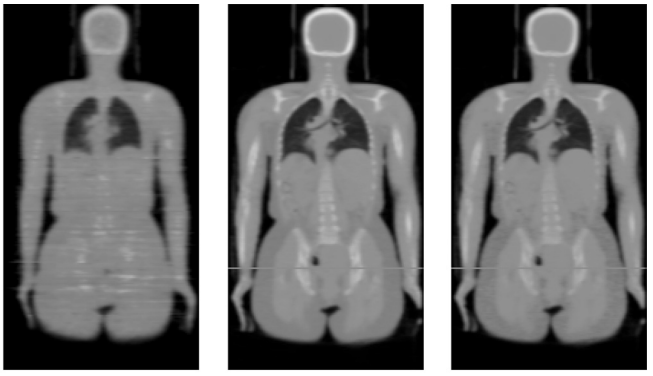

FIG. 6. Attenuation map generated using (a) $^{68}Ge/^{68}Ga$ rod source transmission scan, (b) bilinear, and (c) VDECT methods.

Figure 5 shows typical clinical μ-maps generated using the bilinear, DECT, and VDECT energy-mapping techniques together with the CT image acquired at 140 kV_P. Table I summarizes the mean μ_{511keV} in lung, bone, and soft tissues for each μ-map together with the mean relative difference between both μ-maps when compared to the one obtained using the DECT. Statistical analysis results (P-values were obtained using the Mann–Whitney test) are also presented.

Similarly, typical whole body μ-maps generated using transmission scanning, bilinear, and VDECT energy-mapping techniques are shown in Fig. 6. The mean μ_{511keV} in the lungs, bones, and soft tissues for each μ-map together with the mean relative difference between each μ-map and the transmission image are summarized in Table II.

Correlation plots between each energy-mapping method (bilinear and VDECT) and the reference are shown in Figs. 7 and 8. In lung and soft tissues, both energy-mapping methods provide a good prediction of μ_{511keV}. However, the VDECT achieves a better agreement with reference for bone compared with the bilinear technique.

III.B. Phantom studies

A similar approach was adopted for validation of conversion equations using phantom studies. In the XCAT phantom,

TABLE I. Comparison of calculated μ_{511keV} for clinical studies using the bilinear and VDECT methods with corresponding values obtained using the DECT technique serving as reference.

	DECT	Bilinear			VDECT		
Tissue type	Mean ± SD	Mean ± SD	PRD[a] ± SD (%)	P-value[b]	Mean ± SD	PRD ± SD (%)	P-value
Lung	0.023 ± 0.01	0.027 ± 0.01	16.4 ± 9.7	0.159	0.023 ± 0.01	8.0 ± 8.1	0.468
Soft tissue	0.098 ± 0.00	0.099 ± 0.01	1.6 ± 2.5	0.425	0.097 ± 0.01	2.2 ± 1.8	<0.005
Bone	0.140 ± 0.02	0.153 ± 0.03	8.9 ± 3.9	<0.02	0.138 ± 0.02	1.5 ± 1.2	<0.05

[a]Percentage relative difference.
[b]P-values were obtained using the Mann–Whitney statistical test.

TABLE II. Comparison of calculated μ_{511keV} for clinical whole-body PET/CT studies using the bilinear, DECT, and VDECT methods with corresponding values obtained using the transmission image acquired using $^{68}Ge/^{68}Ga$ rod sources serving as reference.

	Reference	Bilinear			VDECT		
Tissue	Mean ± SD	Mean ± SD	PRD[a] ± SD (%)	P-value[b]	Mean ± SD	PRD ± SD(%)	P-value
Lung	0.025 ± 0.007	0.026 ± 0.008	13.4 ± 10.2	0.021	0.024 ± 0.07	11.8 ± 8.8	0.340
Soft tissue	0.094 ± 0.004	0.100 ± 0.006	7.1 ± 4.6	<0.005	0.099 ± 0.005	5.4 ± 3.7	<0.005
Bone	0.120 ± 0.010	0.141 ± 0.017	17.7 ± 7.3	<0.005	0.129 ± 0.013	8.8 ± 4.1	<0.005

[a]Percentage relative difference.
[b]P-values were obtained using the Mann–Whitney statistical test.

the correlation coefficient resulting from the comparison of the original CT image at 60 keV (effective CT energy at 80 kV_P) derived from the XCAT phantom and the generated VDECT image at the same energy using kV_P conversion equations is very close to the unity (0.98). Similar observations were made for the polyethylene phantom where the correlation coefficient is equal to 0.96.

The estimated μ_{511keV} using the 3 energy-mapping approaches at 511 keV and the actual coefficients together with the percentage relative differences for various tissues are summarized in Table III. All the energy-mapping methods yield acceptable performance in lung and soft tissues. However, in bone tissues, the mean relative difference between theoretical and calculated attenuation coefficients for bilinear, DECT, and VDECT methods is 11.8%, 3.0%, and 2.8%, respectively. Hence, the proposed technique improves the accuracy of computed μ-map at 511 keV in comparison with the bilinear method, which is implemented on commercial PET/CT scanners, especially in bone tissues. The conversion curves relating CT numbers at 140 kVp to attenuation coefficients at 511 keV are plotted in Fig. 9 for the bilinear and VDECT methods as well as the reference derived from the XCAT phantom. The proposed method has better agreement with the reference especially in bone tissue.

Table IV summarizes μ_{511keV} obtained using the bilinear, VDECT, and DECT methods together with the mean percentage relative difference for different concentrations of K_2HPO_4. The mean relative difference between actual and calculated attenuation coefficients when using the bilinear, VDECT, and DECT approaches are 9.5%, 4.0%, and 4.0%, respectively. The original CT image at 140 kV_P and generated μ-maps using different energy-mapping approaches is shown in Fig. 10.

The ROI analysis of PET images corrected for attenuation using the bilinear, DECT, and VDECT methods is shown in Table V. The mean relative differences are 6.4%, 6.5%, and

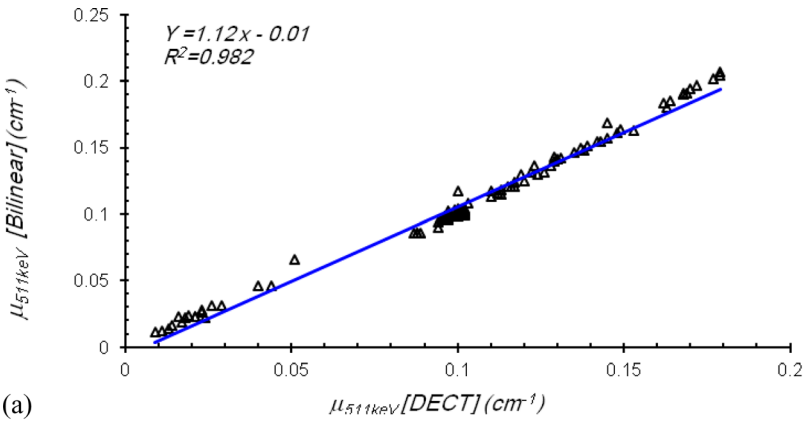

(a)

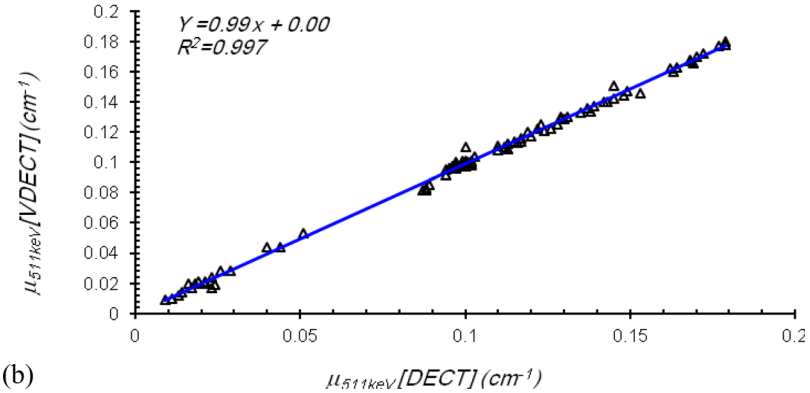

(b)

FIG. 7. Correlation plots between (a) bilinear and DECT, and (b) VDECT and DECT energy-mapping approaches.

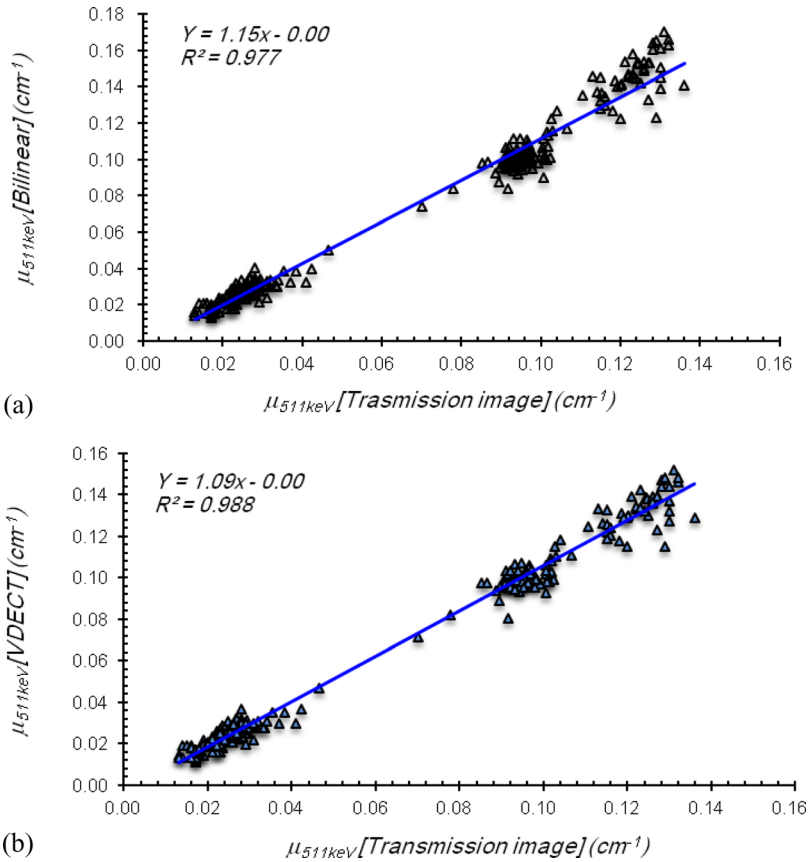

FIG. 8. Correlation plots between ^{68}Ge/^{68}Ga transmission scan serving as reference and (a) bilinear and (b) VDECT energy-mapping approaches.

13.4% for the DECT, VDECT, and bilinear approaches, respectively. Thus, the proposed method is more accurate than the bilinear technique. The attenuation corrected PET images using the bilinear and VDECT energy-mapping methods and the original XCATs μ-map at 511 keV are shown in Fig. 11.

IV. DISCUSSION

The aim of this study is to propose a novel energy-mapping method to improve the accuracy of attenuation correction compared to the standard bilinear technique used on clinical PET/CT scanners. It should be noted that although the bilinear approach provides an acceptable accuracy in lung and soft tissues, it slightly overestimates $\mu_{511\text{keV}}$.[17] The proposed method is based on the dual-energy formulation[18,19] but requires only one CT image acquired at a single kV_P for its implementation.

In comparison with the bilinear method, the proposed technique has better agreement with the dual-energy approach, recognized as the most accurate method, especially for bone (Table I and Fig. 7). The statistical analysis did not reveal any statistically significant difference between DECT and the bilinear technique for lung and soft tissues, whereas statistically significant difference is demonstrated for bone (P-value < 0.05). In addition, there is a statistically

TABLE III. Comparison between actual and $\mu_{511\text{keV}}$ for the XCAT phantom obtained using the bilinear, DECT, and VDECT energy-mapping approaches for different biological tissues. The percentage relative differences (%) for each method are also shown.

Tissue	Actual $\mu_{511\text{keV}}$[a]	Bilinear (PRD%)	DECT (PRD%)	VDECT (PRD%)
Lung	0.0267	0.0277 (3.8)	0.0278 (4.1)	0.0251 (5.9)
Body (water)	0.0927	0.0965 (4.1)	0.0966 (4.2)	0.0961 (3.6)
Brain	0.0963	0.0995 (3.3)	0.0999 (3.7)	0.0981 (1.8)
Muscle	0.0968	0.0999 (3.2)	0.1004 (3.8)	0.0984 (1.6)
Kidney	0.0968	0.1000 (3.3)	0.1005 (3.9)	0.0984 (1.7)
Heart	0.0969	0.1000 (3.2)	0.1006 (3.8)	0.0984 (1.6)
Blood	0.0976	0.1009 (3.4)	0.1014 (3.9)	0.0991 (1.5)
Liver	0.0977	0.1007 (3.1)	0.1014 (3.8)	0.0989 (1.3)
Cartilage	0.1008	0.1043 (3.5)	0.1047 (3.8)	0.1014 (0.6)
Spine bone	0.1101	0.1198 (8.8)	0.1134 (3.0)	0.1124 (2.1)
Rib bone	0.1305	0.1491 (14.2)	0.1345 (3.1)	0.1352 (3.6)

[a]Derived from XCATs attenuation map at 511 keV.

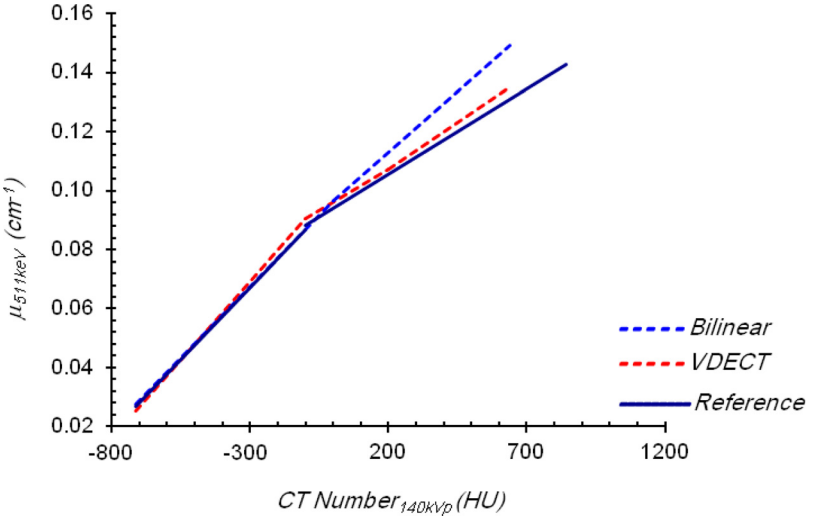

FIG. 9. Plots of conversion curves for the bilinear and VDECT energy-mapping approaches together with the reference derived from the XCAT phantom.

significant difference between DECT and VDECT methods for soft tissue (P-value < 0.005), whereas no proof of statistically significant difference was observed for lung and bone.

For the clinical PET/CT studies, the proposed method outperforms the bilinear technique in comparison with transmission images acquired using ^{68}Ge/^{68}Ga rod sources (Table II and Fig. 8). The statistical analysis did not reveal any statistically significant difference between transmission images and μ-maps generated using the bilinear approach for lung tissue, whereas statistically significant difference is demonstrated for bone and soft tissues (P-value < 0.005). In addition, there is a statistically significant difference between the transmission image and VDECT μ-maps for bone and soft tissues (P-value < 0.005), whereas no proof of statistically significant difference was observed for lung.

Similarly, the XCAT phantom studies seem to indicate that all energy-mapping methods provide similar performance for prediction of μ_{511keV} in lung and soft tissues. The largest absolute difference in μ_{511keV} calculated using the three methods is 0.0033 cm^{-1}. Hence, the differences in lung and soft tissues are almost negligible. However, both the DECT and the proposed VDECT method present better agreement with the reference μ-map for bone. It is worth noting that the estimated linear attenuation coefficients and calculated percentage relative differences for the VDECT approach are almost similar to corresponding values for the

TABLE IV. Comparison between μ_{511keV} obtained using the different energy-mapping approaches and the corresponding values computed using the XCOM photon cross-section library (Ref. 24) for various concentrations of K_2HPO_4 within the polyethylene phantom. The percentage relative differences (%) are also shown for each method.

	μ_{511keV} (cm^{-1}) (PRD%)			
C[a] (mgr/cc)	Reference[b]	Bilinear	DECT	VDECT
Air	0.0	0.028 (-)	0.029 (-)	0.026 (-)
Water	0.096	0.096 (0.0)	0.097 (1.0)	0.095 (0.0)
120	0.102	0.107 (4.9)	0.105 (2.9)	0.103 (2.0)
180	0.106	0.113 (6.6)	0.105 (0.9)	0.107 (1.9)
240	0.109	0.121 (11.0)	0.115 (3.7)	0.114 (5.5)
300	0.112	0.126 (12.5)	0.118 (4.5)	0.117 (4.5)
360	0.116	0.131 (12.9)	0.122 (4.3)	0.122 (4.3)
480	0.123	0.140 (13.8)	0.128 (4.1)	0.128 (4.9)
540	0.126	0.144 (14.3)	0.131 (3.2)	0.131 (4.0)
600	0.129	0.148 (14.2)	0.133 (3.1)	0.134 (3.9)
660	0.133	0.153 (15.0)	0.137 (2.3)	0.138 (4.5)
720	0.136	0.157 (15.4)	0.139 (2.2)	0.141 (3.7)
840	0.143	0.163 (14.0)	0.142 (0.0)	0.146 (2.8)
900	0.147	0.165 (12.9)	0.144 (1.4)	0.148 (0.7)
1200	0.164	0.179 (9.8)	0.153 (6.1)	0.159 (3.7)
1500	0.181	0.188 (3.9)	0.159 (12.1)	0.166 (8.3)
1800	0.199	0.198 (0.5)	0.165 (15.6)	0.173 (12.6)
PRD (%) Mean ± SD	—	9.5 ± 5.6	4.0 ± 4.1	4.0 ± 3.1

[a]Concentration of K_2HPO_4 solution.
[b]Reference values calculated using the XCOM photon cross-section library.

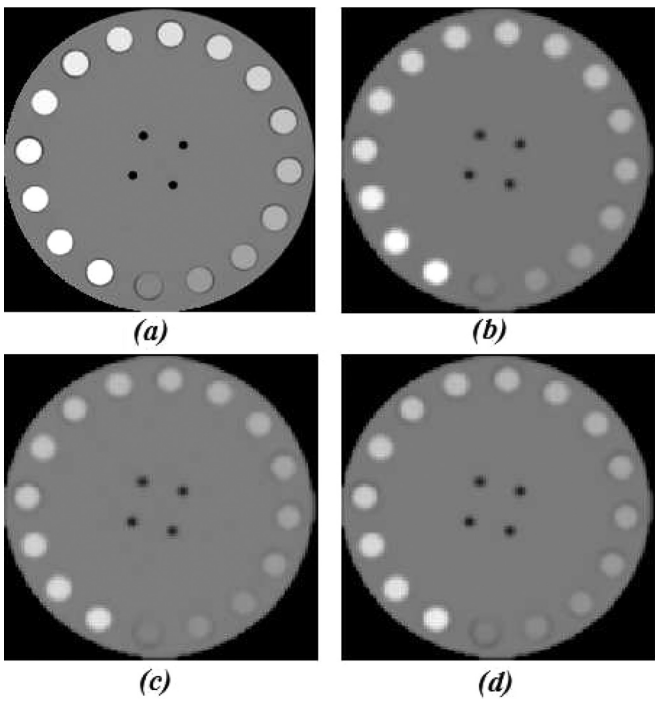

FIG. 10. (a) Original CT image and generated attenuation maps using (b) bilinear, (c) DECT, and (d) VDECT energy-mapping approaches.

TABLE V. Activity ratios for various regions defined on reconstructed PET images of the XCAT phantom corrected for attenuation using the bilinear, DECT, and VDECT μ-maps. The percentage relative differences (%) with respect to the reference for each method are also shown.

	Activity ratios (PRD%)			
Tissue	Reference	Bilinear	DECT	VDECT
Lung	0.526	0.532 (1.1)	0.542 (3.0)	0.475 (9.7)
Blood	1.101	1.248 (13.4)	1.144 (3.9)	1.156 (5.0)
Body	1.509	1.748 (15.8)	1.627 (7.8)	1.706 (13.1)
Spine	1.964	2.628 (33.8)	2.238 (14.0)	2.139 (8.9)
Kidney	3.015	3.399 (12.7)	3.157 (4.7)	3.169 (5.1)
Liver	2.991	3.366 (12.5)	3.105 (3.8)	3.144 (5.1)
Spleen	2.998	3.374 (12.5)	3.129 (4.4)	3.197 (6.6)
Myocardium	3.672	4.118 (12.1)	4.040 (10.0)	3.843 (4.7)
L-Lung[a]	15.23	16.993 (11.6)	16.230 (6.6)	15.89 (4.3)
L-Scapula	20.548	23.185 (12.8)	22.220 (8.1)	21.326 (3.8)
L-Spine	12.938	14.475 (11.9)	13.284 (2.7)	13.689 (5.8)
L-Kidney	39.443	44.306 (12.3)	42.380 (7.4)	41.526 (5.3)
L-Liver	31.371	35.137 (12.0)	33.503 (6.8)	33.517 (6.8)
PRD (%) Mean ± SD		13.4 ± 6.7	6.4 ± 3.2	6.5 ± 2.5

[a]"L-Organ" represents a lesion defined in the considered organ.

DECT approach. The small difference (0.2%) between the both energy-mapping techniques is almost negligible. The bilinear approach led to a larger deviation compared to other methods (Table III). For some tissues, the PRDs for the VDECT approach are less than the corresponding values for the DECT technique serving as reference. This is likely due to statistical noise[28] and the simplicity of the simulation procedure, although relevant to the methodology presented.

The conversion curve produced using the proposed method has better agreement with the reference derived from the XCAT phantom compared to the bilinear approach especially in bone (Fig. 9). The results of the polyethylene phantom studies are consistent with the observations made for the clinical and XCAT phantom studies. The proposed method yields similar results to the DECT technique whereas the bilinear approach presents much higher relative differences compared to the VDECT and DECT approaches especially in regions of high concentrations of K_2HPO_4 (Table IV).

Reconstructed PET images of phantom studies corrected for attenuation using the VDECT method yielded a higher quantitative accuracy with respect to the bilinear method (Table V and Fig. 11). Overall, the differences between various energy-mapping techniques are more pronounced in μ-maps than reconstructed PET images. This is in agreement with observations made in previous studies reporting on the assessment of the impact of variations in the attenuation map on attenuation corrected PET images.[17,29,30]

Novel x-ray tube technologies, allowing switching the kV_P slice by slice, can also be used for implementation of the DECT technique. However, the main drawback of this technology is the deep level of ruination of the x-ray tube during switching. Since such x-ray tubes are not yet commonly used on commercially available PET/CT scanners, the derivation of accurate μ-maps is still an area of considerable research interest.

In similar studies, iterative image reconstruction methods based on accurate physical and statistical models were used to suppress noise, thus enabling the use of low-dose DECT.[19,31] The main drawbacks of these methods are the associated complexity and computational time. Also in some patients, mismatches are expected between CT images acquired at different kV_Ps owing to patient motion. The approach proposed in this work enables the implementation of the DECT technique by maintaining its advantages and keeping the dose to the patient unchanged compared to conventional CTAC. It is recognized that the results presented so far were obtained in the absence of contrast agents or metallic objects since the method combines a single energy CT scan with conversion equations to virtually generate a second CT image which makes it difficult to discriminate between contrast agents and bone. We plan to exploit segmentation algorithms to distinguish regions belonging to contrast media[32] or metallic objects[30] in CT images and use dedicated conversion curves to generate virtual images corresponding to these regions. This scheme is being refined and further developed and will be assessed carefully using clinical PET/CT studies.

It is worth noting that since noise is lower for CT images acquired at 140 kV_P, the CT image at 140 kV_P is used for generation of the second CT image at 80 kV_P, allowing implementation of a novel energy-mapping approach taking advantage of the DECT technique. The combination of 80 and 140 kV_P results in a more accurate μ-map compared to any other energy combination.[17]

V. CONCLUSION

This work demonstrates that the proposed VDECT approach for energy mapping performs better than the bilinear method implemented on commercial PET/CT scanners, especially for bone. More importantly, it achieves similar performance compared to the DECT approach, recognized

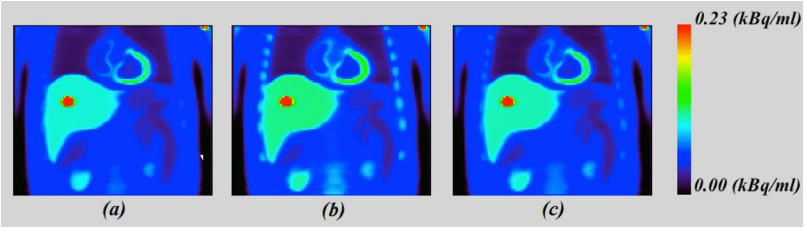

FIG. 11. Attenuation corrected PET images using (a) the actual XCAT phantom, (b) bilinear, and (c) VDECT attenuation maps.

as the most accurate technique available today. A significant advantage of the proposed technique is that no additional dose to the patient is required, which is an important issue for the pediatric population and for all studies when patient dose is a concern. It is recognized that the presented results were obtained in the absence of the contrast agents and metallic implants. The algorithm is being refined to consider these issues.

ACKNOWLEDGMENTS

This work was supported by Tehran University of Medical Sciences under Grant No. 10907, the Swiss National Science Foundation under Grant No. 31003A-135576, Geneva Cancer League and the Indo-Swiss Joint Research Programme ISJRP 138866. The authors are indebted to Dr. A. Rahmim (Johns Hopkins Medical Institutions) for providing clinical studies acquired on the Discovery LS PET/CT scanner.

APPENDIX A

For the energies of interest in diagnostic imaging, the total linear attenuation coefficient (μ^{tot}) is the sum of the photoelectric (μ^{pe}) and Compton (μ^{c}) components

$$\mu^{tot} = \mu^{pe} + \mu^{c}. \tag{A1}$$

The photoelectric component is given by

$$\mu^{pe} = K(E)^{-3}, \tag{A2}$$

where K is a constant and E is the photon energy.

The total Compton attenuation coefficient is given by the Klein-Nishina formula

$$\mu^{c} = X\left[\frac{2(1+\alpha)^2}{\alpha^2(1+2\alpha)} + \frac{\ln(1+2\alpha)}{\alpha}\left(\frac{1}{2} - \frac{1+\alpha}{\alpha^2}\right) - \frac{1+3\alpha}{(1+2\alpha)^2}\right], \tag{A3}$$

where $\mathbf{X} = \frac{3\mathbf{n}_e\sigma^0}{4}$, $\alpha = \frac{E}{m_e c^2}$, and σ^0 is the classical cross section. Therefore, two incident photon beams with energies of 60 and 82 keV (corresponding to the effective CT energy at 80 $\mathrm{kV_P}$ and 140 $\mathrm{kV_P}$, respectively) having corresponding attenuation coefficients of $\mu_{60\mathrm{keV}}$ and $\mu_{82\mathrm{keV}}$, respectively, the total linear attenuation coefficient ($\mu_{511\mathrm{keV}}$) at an energy of 511 keV is given by

$$\mu_{511keV} = 0.9521\mu_{82keV} - 0.3729\mu_{60keV}, \tag{A4}$$

where $\mu_{82\mathrm{keV}}$ is obtained from the CT image at 140 $\mathrm{kV_P}$ and $\mu_{60\mathrm{keV}}$ is calculated using the $\mathrm{kV_P}$ conversion equations for each tissue type as follows:

$$\text{Lung tissue}: \mu_{60keV} = 1.2252\mu_{82keV} + 0.0023, \tag{A5}$$

$$\text{Soft tissue}: \mu_{60keV} = 1.7068\mu_{82keV} - 0.1022, \tag{A6}$$

$$\text{Bone tissue}: \mu_{60keV} = 1.6191\mu_{82keV} - 0.0820. \tag{A7}$$

Using Eqs. (A5)–(A7) and Eq. (A4) could be rewritten for each tissue type

$$\text{Lung tissue}: \mu_{511keV} = 0.4952\mu_{82keV} - 0.0009, \tag{A8}$$

$$\text{Soft tissue}: \mu_{511keV} = 0.3156\mu_{82keV} + 0.0381, \tag{A9}$$

$$\text{Bone tissue}: \mu_{511keV} = 0.3483\mu_{82keV} + 0.0301. \tag{A10}$$

[a]Author to whom correspondence should be addressed. Electronic mail: mohammadreza_ay@tums.ac.ir; Telephone: +98 21 66466383; Fax: +98 21 66402729.

[1]H. Zaidi and K. F. Koral, "Scatter modelling and compensation in emission tomography," Eur. J. Nucl. Med. Mol. Imaging **31**(5), 761–782 (2004).
[2]M. Osman, C. Cohade, Y. Nakamoto, and R. Wahl, "Respiratory motion artifacts on PET emission images obtained using CT attenuation correction on PET-CT," Eur. J. Nucl. Med. Mol. Imaging **30**(4), 603–606 (2003).
[3]H. Zaidi and B. Hasegawa, "Determination of the attenuation map in emission tomography," J. Nucl. Med. **44**(2), 291–315 (2003).
[4]O. Rousset, A. Rahmim, A. Alavi, and H. Zaidi, "Partial volume correction strategies in PET," PET Clin. **2**(2), 235–249 (2007).
[5]A. Braem, M. Llatas, E. Chesi, J. Correia, F. Garibaldi, C. Joram, S. Mathot, E. Nappi, M. da Silva, F. Schoenahl, J. Seguinot, P. Weilhammer, and H. Zaidi, "Feasibility of a novel design of high resolution parallax-free Compton enhanced PET scanner dedicated to brain research," Phys. Med. Biol. **49**(12), 2547–2562 (2004).
[6]A. Sanchez-Crespo, P. Andreo, and S. Larsson, "Positron flight in human tissues and its influence on PET image spatial resolution," Eur. J. Nucl. Med. Mol. Imaging **31**(1), 44–51 (2004).
[7]K. Shibuya, E. Yoshida, F. Nishikido, T. Suzuki, T. Tsuda, N. Inadama, T. Yamaya, and H. Murayama, "Annihilation photon acollinearity in PET: Volunteer and phantom FDG studies," Phys. Med. Biol. **52**(17), 5249–5261 (2007).
[8]M. Lonneux, I. Borbath, A. Bol, A. Coppens, M. Sibomana, R. Bausart, M. Defrise, S. Pauwels, and C. Michel, "Attenuation correction in whole-body FDG oncological studies: The role of statistical reconstruction," Eur. J. Nucl. Med. **26**(6), 591–598 (1999).
[9]C. Bai, P. E. Kinahan, D. Brasse, C. Comtat, D. W. Townsend, C. C. Meltzer, V. Villemagne, M. Charron, and M. Defrise, "An analytic study of the effects of attenuation on tumor detection in whole-body PET oncology imaging," J. Nucl. Med. **44**(11), 1855–1861 (2003).
[10]P. E. Kinahan, D. W. Townsend, T. Beyer, and D. Sashin, "Attenuation correction for a combined 3D PET/CT scanner," Med. Phys. **25**(10), 2046–2053 (1998).
[11]P. E. Kinahan, B. H. Hasegawa, and T. Beyer, "X-ray-based attenuation correction for positron emission tomography/computed tomography scanners," Semin. Nucl. Med. **33**(3), 166–179 (2003).
[12]H. Zaidi, "Is radionuclide transmission scanning obsolete for dual-modality PET/CT systems?," Eur. J. Nucl. Med. Mol. Imaging **34**(6), 815–818 (2007).
[13]R. Alvarez and A. Macovski, "Energy-selective reconstructions in x-ray computerized tomography," Phys. Med. Biol. **21**(5), 733–744 (1976).
[14]C. Bai, L. Shao, A. J. Da Silva, and Z. Zhao, "A generalized model for the conversion from CT numbers to linear attenuation coefficients," IEEE Trans. Nucl. Sci. **50**(5), 1510–1515 (2003).
[15]T. Beyer, P. E. Kinahan, D. W. Townsend, and D. Sashin, "The use of x-ray CT for attenuation correction of PET data," presented at the *Proceedings of IEEE Nuclear Science Symposium and Medical Imaging Conference*, 30 Oct.–5 Nov., Norfolk, VA, pp. 1573–1577 (1994).
[16]C. Burger, G. Goerres, S. Schoenes, A. Buck, A. Lonn, and G. Von Schulthess, "PET attenuation coefficients from CT images: Experimental evaluation of the transformation of CT into PET 511-keV attenuation coefficients," Eur. J. Nucl. Med. Mol. Imaging **29**(7), 922–927 (2002).
[17]M. R. Ay, M. Shirmohammad, S. Sarkar, A. Rahmim, and H. Zaidi, "Comparative assessment of energy-mapping approaches in CT-based attenuation correction for PET," Mol. Imaging Biol. **13**(1), 187–198 (2011).
[18]M. J. Guy, I. A. Castellano-Smith, M. A. Flower, G. D. Flux, R. J. Ott, and D. Visvikis, "DETECT-dual energy transmission estimation CT-for improved attenuation correction in SPECT and PET," IEEE Trans. Nucl. Sci. **45**(3), 1261–1267 (1998).
[19]P. E. Kinahan, A. M. Alessio, and J. A. Fessler, "Dual energy CT attenuation correction methods for quantitative assessment of response to cancer therapy with PET/CT imaging," Technol. Cancer Res. Treat. **5**(4), 319–327 (2006).

[20]C. C. Watson, V. Rappoport, D. Faul D, D. W. Townsend, and J. P. Carney, "A method for calibrating the CT-based attenuation correction of PET in human tissue," IEEE Trans. Nucl. Sci. **53**, 102–107 (2006).
[21]B. Teimourian, M. R. Ay, H. Ghadiri, M. S. Zafarghandi, and H. Zaidi, "A novel approach for implementation of dual energy mapping technique in CT-based attenuation correction using single kVP imaging: A feasibility study," presented at the *XII Mediterranean Conference on Medical and Biological Engineering and Computing 2010* (Chalkidiki, Greece, 2010), pp. 220–223.
[22]ICRU, "Tissue substitutes in radiation dosimetry and measurement," Report No. 44, 1989.
[23]A. M. Loening and S. S. Gambhir, "AMIDE: A free software tool for multimodality medical image analysis," Mol. Imaging **2**(3), 131–137 (2003).
[24]M. J. Berger, J. H. Hubbell, S. M. Seltzer, J. Chang, J. S. Coursey, and R. Sukumar, XCOM: photon cross sections database, 1998. Report NBSIR 87-3597. Gaithersburg: Ionizing Radiation Division, Physics Laboratory, National Institute of Standards and Technology, Gaithersburg, MD 20899. Available at http://physics.nist.gov/PhysRefData/Xcom/Text/XCOM.html.
[25]W. P. Segars, M. Mahesh, T. J. Beck, E. C. Frey, and B. M. Tsui, "Realistic CT simulation using the 4D XCAT phantom," Med. Phys. **35**(8), 3800–3808 (2008).
[26]K. Thielemans, C. Tsoumpas, S. Mustafovic, T. Beisel, P. Aguiar, N. Dikaios, and M. W. Jacobson, "STIR: software for tomographic image reconstruction release 2," Phys. Med. Biol. **57**(4), 867–883 (2012).
[27]J. Bland and D. Altman, "Statistical methods for assessing agreement between two methods of clinical measurement," Lancet **1**(8476), 307–310 (1986).
[28]T. Xia, A. M. Alessio, and P. E. Kinahan, "Noise and bias properties of monoenergetic images from DECT used for attenuation correction with PET/CT and SPECT/CT," Proc. Soc. Photo-Opt. Instrum. Eng. **7622**, 762225 (2010).
[29]M. Ay and H. Zaidi, "Computed tomography-based attenuation correction in neurological positron emission tomography: Evaluation of the effect of x-ray tube voltage on quantitative analysis," Nucl. Med. Commun. **27**, 339–346 (2006).
[30]M. Abdoli, M. Ay, A. Ahmadian, R. Dierckx, and H. Zaidi, "Reduction of dental filling metallic artefacts in CT-based attenuation correction of PET data using weighted virtual sinograms optimized by a genetic algorithm," Med. Phys. **37**(12), 6166–6177 (2010).
[31]J. Noh, J. A. Fessler, and P. E. Kinahan, "Statistical sinogram restoration in dual-energy CT for PET attenuation correction," IEEE Trans. Med. Imaging **28**(11), 1688–1702 (2009).
[32]A. Ahmadian, M. R. Ay, J. H. Bidgoli, S. Sarkar, and H. Zaidi, "Correction of oral contrast artifacts in CT-based attenuation correction of PET images using an automated segmentation algorithm," Eur. J. Nucl. Med. Mol. Imaging **35**(12), 1812–1823 (2008).